ENVIRONMENTAL RESEARCH
LETTERS

LETTER • OPEN ACCESS

Reduction in human activity can enhance the urban heat island: insights from the COVID-19 lockdown

ENVIRONMENTAL RESEARCH
LETTERS

OPEN ACCESS

RECEIVED
10 October 2020

REVISED
20 February 2021

ACCEPTED FOR PUBLICATION
17 March 2021

PUBLISHED
10 May 2021

LETTER

Reduction in human activity can enhance the urban heat island: insights from the COVID-19 lockdown

TC Chakraborty[1], Chandan Sarangi[2,3,*] and Xuhui Lee[1,*]

[1] School of the Environment, Yale University, New Haven, CT 06511, United States of America
[2] Department of Civil Engineering, Indian Institute of Technology Madras, Chennai, Tamil Nadu 600036, India
[3] Laboratory for Atmospheric and Climate Sciences, Indian Institute of Technology Madras, Chennai 600036, India
* Authors to whom any correspondence should be addressed.

E-mail: chandansarangi@civil.iitm.ac.in **and** xuhui.lee@yale.edu

Keywords: urban heat island, COVID-19 lockdown, satellite remote sensing, human–atmosphere–biosphere interactions

Supplementary material for this article is available online

Abstract

The COVID-19 lockdowns drastically reduced human activity, emulating a controlled experiment on human–land–atmosphere coupling. Here, using a fusion of satellite and reanalysis products, we examine this coupling through changes in the surface energy budget during the lockdown (1 April to 15 May 2020) in the Indo-Gangetic Basin, one of the world's most populated and polluted regions. During the lockdown, the reduction (>10%) in columnar air pollution compared to a five year baseline, expected to increase incoming solar radiation, was counteracted by a ∼30% enhancement in cloud cover, causing little change in available energy at the surface. More importantly, the delay in winter crop harvesting during the lockdown increased surface vegetation cover, causing almost half the regional cooling via evapotranspiration. Since this cooling was higher for rural areas, the daytime surface urban heat island (SUHI) intensity increased (by 0.20–0.41 K) during a period of reduced human activity. Our study provides strong observational evidence of the influence of agricultural activity on rural climate in this region and its indirect impact on the SUHI intensity.

1. Introduction

Human-induced changes in the Earth's surface climate have traditionally been difficult to constrain [1, 2], particularly since these changes typically occur at time scales similar to natural decadal perturbations. In contrast, the COVID-19 lockdowns—the restrictions placed by various governing bodies as a response to the COVID-19 pandemic in 2020—caused unprecedented slowdown in human activity [3], were short in duration, and yet intense enough to produce measurable effects. They can thus serve as natural experiments on the anthropogenic control on surface climate.

An ideal study area to explore the results of this perturbation experiment is the Indo-Gangetic Basin (IGB), one of the most densely populated regions on the planet with high levels of air pollution [4]. Covering the majority of North India, the IGB has a subtropical monsoon climate, and is a global hot spot for land–atmosphere coupling [5]. From late March to end of May, a countrywide lockdown was imposed in India as a response to COVID-19. This lockdown strictly restricted people's movement outside their homes, suspended educational, industrial, and hospitality services, and limited all transportation systems [6].

Being both heavily cultivated and rapidly urbanizing [7, 8], the IGB is strongly influenced by anthropogenic changes in land use and land cover [9, 10]. Human influence on surface climate is distinct for urban and rural areas. Urbanization modifies the biophysical properties of the surface due to replacement of natural landscapes with built-up structures. Consequently, cities are usually characterized by higher temperatures compared to their surroundings—the urban heat island (UHI) effect [11]. The UHI is commonly calculated as the temperature difference between the city and a non-standard rural area around the city. Rural areas are influenced

by land use and land management practices, which is primarily due to agriculture in this region.

The reduction in atmospheric aerosols during the lockdown (up to 45% reduction for some Indian states) is well-documented [12] and, all else remaining constant, would increase incoming surface radiation. Since urban and rural areas may have different levels of pollution, this radiative forcing change can impact the UHI intensity [13, 14]. However, the UHI, and surface climate in general, is also modulated by non-radiative pathways [15]. The lockdown restrictions delayed crop harvesting [16], which would allow the rural surfaces to maintain high vegetation cover and can enhance latent heat flux (λE), a non-radiative pathway of surface heat dissipation. Previous studies have noted that the seasonality of the UHI in this region is influenced by the variability in surface vegetation in the rural area [17, 18]. Agricultural influence on surface climate in this region is not well-captured by land-surface models due to inaccurate representation of vegetation properties and the poorly constrained influence of irrigation on the hydrological cycle [10, 19]. Thus, beyond the widely studied changes in atmospheric composition [20, 21], the lockdowns provide a unique opportunity to ask broader questions about human–land–atmosphere interactions in the IGB. For example, the role of these interactions in modulating the ensuing South Asian monsoon circulations is critical to the livelihood of over a billion people dependent on this region [22].

Here, we examine the changes in the surface temperature in the IGB during the lockdown with a focus on the UHI, allowing us to separate human influence on urban and rural surface climate, particularly due to air pollution and land use. First, using a suite of satellite observations, we isolate changes in atmospheric and surface properties over urban areas and their rural periphery. Second, since satellite observations are restricted by the presence of clouds and do not directly provide estimates of the surface energy budget, we use a reanalysis dataset to gain a mechanistic understanding of the observed perturbations in rural surface climate.

2. Materials and methods

2.1. Urban–rural Delineations for region of interest

We only consider the Indian portion of the IGB (figure S1(a); ∼50 000 km^2 (available online at stacks.iop.org/ERL/16/054060/mmedia)), to avoid uncertainties arising from variations in lockdown periods in other countries. An urban cluster database was developed for this region by generating polygons covering contiguous groups of high-density urban pixels from the Global Human Settlement Index for 2015 [23]. The corresponding normalized rural reference (roughly equal to area of urban cluster) for each of these clusters was created using an iterative buffering procedure with a step size of 300 m. Our methodology generates 1420 urban–rural delineations for the region.

2.2. Satellite observations

Multiple satellite-derived products were used to extract urban–rural differentials in relevant variables (details in table 1), including land surface temperature (LST) for calculating surface UHI (SUHI) [24], reflectance data from Moderate Resolution Imaging Spectroradiometer (MODIS) to estimate surface vegetation [25], and metrics of air pollution, including aerosol optical depth (AOD) from MODIS [26] and individual pollutant estimates from the Sentinel-5P TROPOspheric Monitoring Instrument (TROPOMI) sensor [27]. We also extract cloud fraction (CF) from Sentinel-5P since clouds strongly affect the radiative budget and can be higher over cities [28]. Finally, the black-sky albedo (BSA) and white-sky albedo (WSA), the reflectivity of the surface for direct beam and diffuse radiation, respectively, were extracted from MODIS [29]. These can be combined to derive total surface albedo (α; see section 2.3), which is known to vary between urban and rural areas [30]. Although the MODIS observations are daily, the multi-day (see table 1) composites are used to reduce cloud contamination [31].

The normalized difference vegetation index (NDVI) is a proxy for green vegetation [33] and used here to estimate the impact of the lockdown on surface vegetation cover. We calculate NDVI from the near infrared (NIR) and RED bands of the 8 day composite MODIS surface reflectance product, available for 1 km × 1 km grids (table 1), as:

$$\mathrm{NDVI} = \frac{\mathrm{NIR} - \mathrm{RED}}{\mathrm{NIR} + \mathrm{RED}}. \quad (1)$$

The lockdown in India started from midnight 24 March and continued in a limited capacity till 7 June. To remove the noise from the transition periods, we considered 1 April to 15 May 2020 to be the lockdown case. The five year (2015–2019) mean of the data from 1 April to 15 May was treated as the baseline (only 1 April to 15 May 2019 for TROPOMI due to data unavailability). Since the satellite observations are relatively coarse (see table 1), only urban clusters with an area of above 10 km^2 were considered. This threshold, along with cloud screening, leaves 382 clusters for the MODIS and Sentinel-derived CF data (figure S2) and 302 clusters for the Sentinel-derived air pollutant data.

Urban and rural means of all the variables of interest were extracted after regridding to 300 m European Space Agency Climate Change Initiative (ESA CCI) grids using the Google Earth Engine platform [34]. The urban values were calculated as the spatial means of all the urban pixels, as defined by the ESA CCI land cover data [32], within an urban

Table 1. Summary of satellite products used in the present study.

Satellite product	Time of interest	Variable(s) of interest	Temporal resolution	Spatial resolution	Reference
MODIS land surface temperature (LST) product (MYD11A2 v006)	2015–2020	Daytime and nighttime LST from Aqua	8 day	1000 m	[24]
MODIS surface reflectance product (MYD09A1 v006)	2015–2020	Reflectances in the near-infrared and red bands	8 day	500 m	[25]
MODIS global albedo (α) product (MCD43A3 v006)	2015–2020	Black sky albedo (BSA) and white sky albedo (WSA)	16 day	500 m	[29]
MODIS aerosol optical depth (AOD) product (MCD19A2.006)	2015–2020	AOD	Daily	1000 m	[26]
Sentinel-5P TROPOMI	2019–2020	Nitrogen dioxide (NO_2), sulfur dioxide (SO_2), ozone (O_3), carbon monoxide (CO), formaldehyde (HCHO), methane (CH_4), and cloud fraction (CF)	2 day	1000 m (downscaled)	[27]
European Space Agency Climate Change Initiative (ESA CCI) land cover data	2018	Land cover	Yearly	300 m	[32]

cluster. The corresponding rural values are the spatial means of the non-urban, non-water pixels (from the ESA data) in the rural references. The urban–rural differential in LST is the SUHI, while for the other variables, we use the subscript $_{\text{urb-rur}}$. We also calculate the averages of each variable (and their differences) weighted by the urban cluster areas. Since larger urban areas are known to have higher SUHI intensity, area weighing gives us regional mean SUHI (versus the urban cluster mean SUHI).

2.3. Reanalysis data

We used two reanalysis products—the European Centre for Medium-Range Weather Forecasts (ECMWF) Reanalysis 5 (ERA5) [35], available at $0.25^\circ \times 0.25^\circ$, and the Modern-Era Retrospective analysis for Research and Applications, Version 2 (MERRA-2) [36], available at $0.5^\circ \times 0.625^\circ$. The five year (2015–2019) mean of the diffuse fraction (k_d) of the ERA5 reanalysis was used to calculate α from BSA and WSA [37] using the equation:

$$\alpha = k_d \text{WSA} + (1 - k_d)\,\text{BSA}. \quad (2)$$

For each case, the centroid of the urban and rural polygons was located and k_d was extracted for the ERA5 grid containing it, similar to [38].

The MERRA-2 reanalysis assimilates bias-corrected satellite observations of aerosols and provides estimates of the aerosol direct radiative effect, making it ideal for studying the impacts of the COVID-19 lockdowns. Though MERRA-2 also includes estimates of k_d, inter-reanalysis evaluations show that it significantly underestimates k_d compared to other products [39]. Thus, MERRA-2 data were not used to calculate α. Instead, MERRA-2 was used to get all-sky estimates of perturbations in the surface and atmospheric variables (since satellites only provide clear-sky estimates) and to diagnose reasons for perturbations in the rural LST. The MERRA-2 variables were based on hourly data from 12:30 pm to 2:30 pm local time, corresponding to the 1:30 pm MODIS Aqua overpass.

2.4. Statistical analysis

To examine reasons for any potential SUHI change, we considered the temporal changes (Δ, variable value during the lockdown minus value of the reference period) in $\text{AOD}_{\text{urb-rur}}$, $\text{NDVI}_{\text{urb-rur}}$, $\alpha_{\text{urb-rur}}$, and $\text{CF}_{\text{urb-rur}}$ as the predictors. For robustness, we used two methods—linear regressions and random forest (RF) regression. For the linear regressions, we considered each of these four predictors ($\Delta\text{AOD}_{\text{urb-rur}}$, $\Delta\text{NDVI}_{\text{urb-rur}}$, $\Delta\alpha_{\text{urb-rur}}$, and $\Delta\text{CF}_{\text{urb-rur}}$) and all their combinations and subsets. Since the relationships between the predictors and ΔSUHI are not necessarily linear, we also checked the consistency of our results using RF regressions. RF regressions use ensembles of decision trees to detect non-linear relationships and are less sensitive to outliers than parametric linear models [40]. For the RF regression, to prevent overfitting, we trained the models using 70% of the data and checked the model accuracy using the remaining data. The training and accuracy assessment were repeated 50 times with different random splits of training and validation data [41]. The signal can be hard to separate from the noise in the

satellite observations when examining small perturbations. Thus, we also correlate the variables after binning the data into five percentile bins, assuming that this noise is random and contributes to the unexplained variance within bins.

2.5. Intrinsic biophysical mechanism

Since the statistical analyses using satellite observations are primarily for hypothesis generation and do not necessarily reveal the physical mechanisms for the SUHI increase, we employed the theory of Intrinsic Biophysical Mechanism (IBPM) [14, 15, 42, 43], implemented using the MERRA-2 variables [43], to diagnose and quantify the reasons for the change in the LST_{rur} in the region. Conceptually, the total LST change (ΔLST) due to a forcing agent is the sum of the changes in the blending height temperature (ΔBHT), where the blending height is the height at which surface heterogeneity has negligible impact on atmospheric variables [44], and the local temperature response (ΔT):

$$\Delta\mathrm{LST} = \Delta T + \Delta\mathrm{BHT}. \quad (3)$$

ΔBHT is the result of atmospheric factors while ΔT is the surface response to atmospheric forcing. According to the IBPM theory, the local temperature response is:

$$\Delta T = \frac{\lambda_0}{1+f}\Delta K_{\downarrow}(1-a) + \frac{\lambda_0}{1+f}\Delta L + \frac{-\lambda_0}{(1+f)^2}(R_n^* - G)\Delta f_1 + \frac{-\lambda_0}{(1+f)^2} \times (R_n^* - G)\Delta f_2 + \frac{\lambda_0}{1+f}\Delta G. \quad (4)$$

The terms on the right-hand side of equation (4), from left to right, are the contributions to ΔT from shortwave radiative forcing, longwave radiative forcing, energy redistribution through evaporation, energy redistribution through convection, and change in ground heat flux. Here, $\Delta K_{\downarrow}$ is the change in incoming shortwave radiation, ΔL is the change in absorbed longwave radiation, ΔG is the change in ground heat flux, and R_n^* is the apparent net radiation. The intrinsic climate sensitivity is given by λ_0, f is the energy redistribution factor and Δf_1 and Δf_2 are the changes in f due to evaporation and convection, respectively. Check supplementary material for more details.

3. Results

3.1. Changes in urban–Rural differentials during lockdown

The daytime SUHI increased (non-weighted mean from 0.23 K to 0.43 K; area-weighted mean from 0.56 K to 0.97 K) during the COVID-19 lockdown period compared to the five year baseline (figures 1 and S3), with 67% or 257 of the 382 urban clusters showing an increase (figure S4). In contrast, the nighttime ΔSUHI was statistically insignificant (p-value > 0.01). Daytime LST decreased during the lockdown (compared to baseline), though the mean decrease over rural locations was greater (−1.96 K non-weighted; −1.55 K weighted) compared to that over urban regions (−1.76 K non-weighted; −1.14 K weighted).

To explain this differential perturbation in daytime LST_{urb} and LST_{rur}, we consider major atmospheric (CF and AOD) and surface (NDVI and α) factors that impact the SUHI. The air quality over both urban and rural locations improved during the lockdown. This reduced air pollution is evident from both MODIS-derived AOD (∼5%–6% decrease; figures 2(a) and S5(a)) and individual air pollutants measured by TROPOMI (∼14% and ∼19% decrease in urban NO_2 and SO_2, respectively; figure S6). AOD decreases in roughly 67% of the urban clusters (increasing in others) and for most non-urban grids in the IGB (figure S7(a)). The small magnitude of MODIS-derived $AOD_{urb\text{-}rur}$ could be due to the large contributions from natural dust and biomass burning aerosols, as well as occurrence of turbulently mixed deep boundary layers, in this region during this period [45]. Moreover, there was a surprisingly large (>36% for non-weighted; >43% for weighted) increase in CF during the lockdown (figures 2(d) and S5(d)), though some regions show a decrease (figure S7(b)).

We find large (>12%) increases in NDVI during the lockdown period. These increases are generally higher in rural references (13.3% or 0.043) than in urban areas (12.8% or 0.038; figure 2(b)), with $\Delta NDVI_{urb\text{-}rur}$ being negative in ∼59% of the urban clusters (figures S4(b), S7(a), and S8(a)). The positive $\Delta NDVI_{rur}$ (figure S8(b)) is consistent with the impact of the lockdown on agricultural activity, which is the predominant land use for ∼88% of this area according to the ESA CCI data (figure S2(b)). The lockdown overlapped with the harvesting season for rabi (winter) crops, which, together with the drier conditions during this period, reduces surface vegetation during regular years, as can be seen from the moving average of MODIS-derived 8 day $NDVI_{rur}$ in figure 3(c). The delay in harvesting activity [16] may have temporally shifted this normal drop in $NDVI_{rur}$, contributing to surface greening compared to the baseline (figure 3(c)). The $\Delta NDVI_{rur}$ is higher than the inter-annual standard deviation of $NDVI_{rur}$ during this period, also demonstrated by the largest standardized anomalies of the year during the lockdown. Most of IGB shows this surface greening, with $\Delta NDVI_{rur}$, ranging from −0.01 (5th percentile) to 0.11 (95th percentile), as well as a reduction in LST_{rur} (figures 3(a) and (b)) from −4.3 K (5th percentile) to 0.4 K (95th percentile), with the SUHI increasing compared to baseline (figure 3(d)). Simultaneously, α decreased in both urban (−2.6%) and rural (−2.9%)

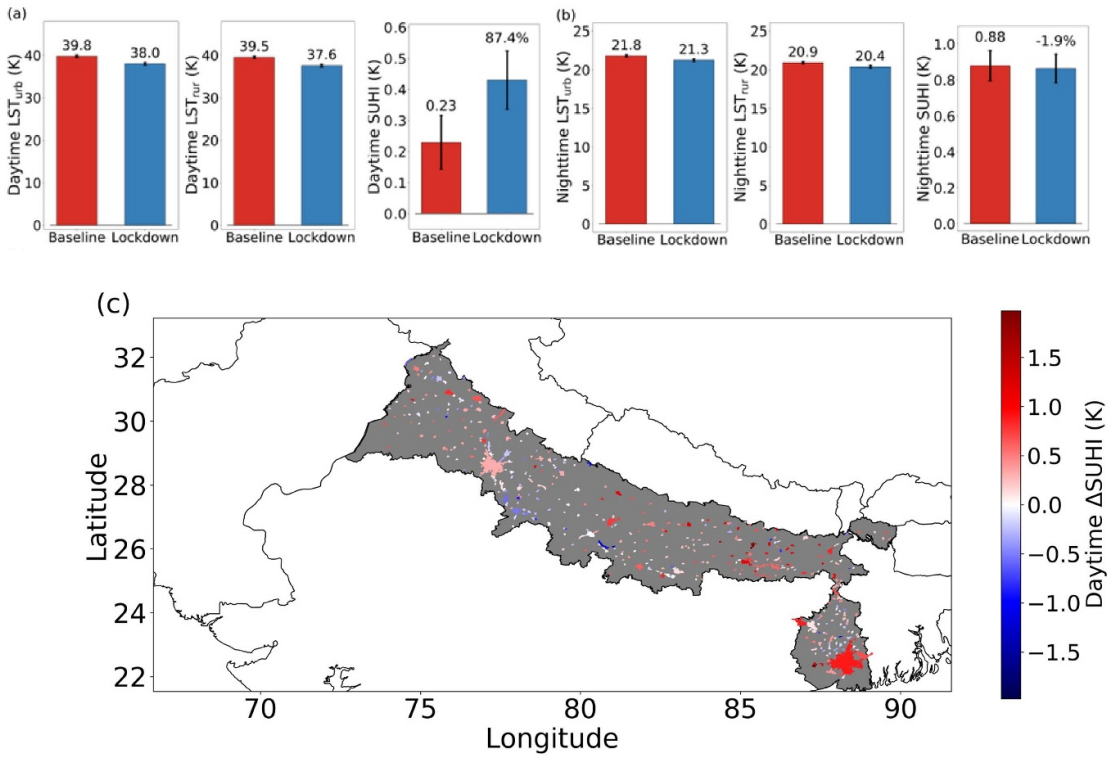

Figure 1. Perturbations to land surface temperature (LST) and surface urban heat island (SUHI) intensity. Sub-figures (a) and (b) show the mean (not weighted by urban cluster area) land surface temperature (LST) and surface urban heat island (SUHI) for urban clusters and their rural references for the baseline period, as well as their perturbed values during the lockdown period, for daytime and nighttime, respectively. The values above the bars show the mean values (percentage change during lockdown period for SUHI) and the error bars represent the 95% confidence interval of the mean. The changes shown here are summarized in table S1. Sub-figure (c) shows a map of the urban clusters in the region of interest and the change in their spatial mean daytime SUHI during the lockdown compared to the five year baseline.

areas (figures 2(c) and S5(c)). Paired two-sample t-tests confirm that all the satellite-observed changes in the variables, other than that for nighttime SUHI, are statistically significant (p-value < 0.01). The 95% confidence intervals for the mean of each variable are in table S1.

3.2. Attribution of daytime SUHI enhancement

Previous studies have shown relationships between $AOD_{urb\text{-}rur}$ and SUHI [13, 14]. Here, we find almost no associations between the perturbations in the two during the lockdown period (figure 4(a); $r^2 = 0.02$ for cluster; not statistically significant for binned). Similarly, $AOD_{urb\text{-}rur}$ and daytime SUHI are not well-correlated during the baseline and lockdown periods (figure S9(b); $r^2 \sim 0$). However, $\Delta NDVI_{urb\text{-}rur}$ shows a relatively strong inverse relationship with ΔSUHI (figure 4(b); $r^2 = 0.16$ for cluster; 0.76 for binned). Given the generally higher $\Delta NDVI_{rur}$, the pause in human activity in the rural area may have contributed to the enhanced daytime SUHI. This impact of urban–rural vegetation differentials on SUHI is consistent with previous studies [46, 47] and is corroborated by the relatively strong associations between $NDVI_{urb\text{-}rur}$ and daytime SUHI for the two periods (figure S9(a)). Although $\Delta\alpha_{urb\text{-}rur}$ shows a positive relationship with ΔSUHI ($r^2 = 0.05$ for cluster; 0.52 for binned), this relationship is not physically possible in isolation, since a higher α implies lower absorption of solar insolation by the surface, and thus, lower ΔSUHI. Since α and NDVI are correlated (figure S10), the positive relationship between $\Delta\alpha_{urb\text{-}rur}$ and ΔSUHI may be a statistical artifact of the relatively higher $NDVI_{rur}$. Neither $CF_{urb\text{-}rur}$ and daytime SUHI intensity, nor their perturbations from the baseline to the lockdown, are correlated (figures 4(d) and S9(c)).

We use multiple linear and RF regressions to provide further statistical robustness to our findings (table S2). In general, $\Delta NDVI_{urb\text{-}rur}$ explains the largest portion of the variability in ΔSUHI (adjusted $R^2 = 0.15$), followed by $\Delta\alpha_{urb\text{-}rur}$, $\Delta AOD_{urb\text{-}rur}$, and $CF_{urb\text{-}rur}$. The permutation importance scores from the RF models also support the primary control of $\Delta NDVI_{urb\text{-}rur}$ on ΔSUHI (table S2).

The percentage changes in the atmospheric variables (AOD and CF) are higher over urban areas compared to the rural areas during the lockdown period and the surface properties (NDVI and α) change more for rural areas (figures 2 and S5). Although 2020 was already wetter than regular years [18], a further reduction in AOD over the study area may

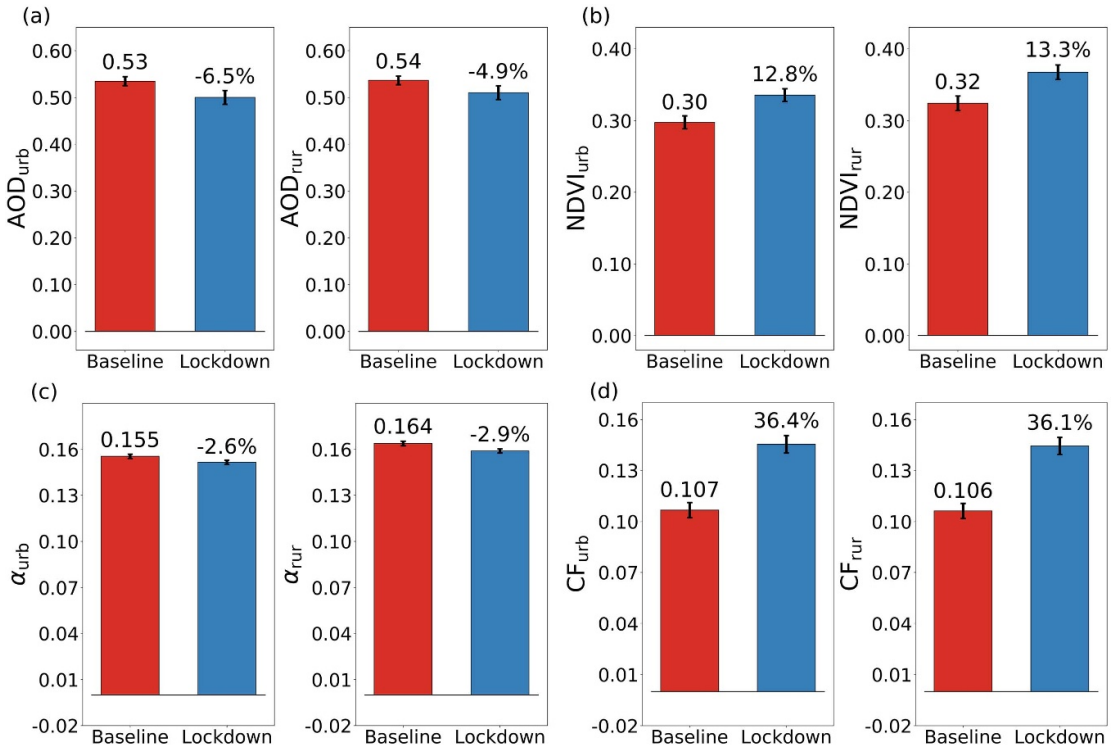

Figure 2. Changes in major surface and atmospheric factors. Sub-figures (a)–(d) show the mean (not weighted by urban cluster area) aerosol optical depth (AOD), normalized difference vegetation index (NDVI), surface albedo (α), and cloud fraction (CF) for urban clusters and their rural references for the baseline period, as well as their perturbed values during the lockdown. The values above the bars show the mean values for the baseline period (2015–2019 baseline for everything other than CF; 2019 baseline for CF) and the percentage change from that value. The error bars represent the 95% confidence interval of the mean. The changes shown here are summarized in table S1.

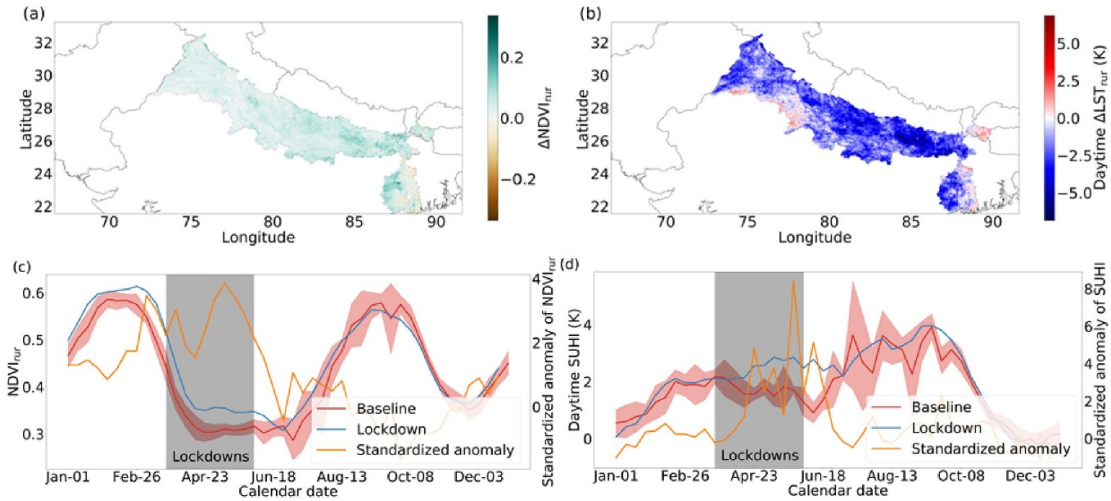

Figure 3. Regional changes in vegetation cover and land surface temperature (LST). Sub-figures (a) and (b) show maps of the changes in rural normalized difference vegetation index ($NDVI_{rur}$) and daytime rural land surface temperature (LST_{rur}) during the lockdown compared to the five year baseline. Sub-figure (c) shows the seasonal change in NDVI for baseline years (2015–2019; in red) and the year 2020 (in blue) over all rural pixels in the study area. The standardized anomaly of $NDVI_{rur}$ (the difference in $NDVI_{rur}$ between the baseline and lockdown divided by the inter-annual standard deviation of $NDVI_{rur}$) for each 8 day period is shown in orange. The red shaded region shows the standard deviation of the baseline value across years, while the grey shaded region shows the overall lockdown period. To reduce noise, the moving average of three points is used to compute the 2020 values. Sub-figure (d) is similar to sub-figure (c), but for seasonal variability of daytime surface urban heat island (SUHI) intensity.

have perturbed the regional circulation and thermodynamics [48, 49], creating an environment conducive to more cloud formation. It may also be possible that the lower aerosol loading reduced the cloud-burning effect [50], thus increasing CF. Finally, the surface greening could also enhance CF [51]. We expect a greater decrease in AOD over urban clusters to correspond to an increase in $K_{\downarrow}$, which

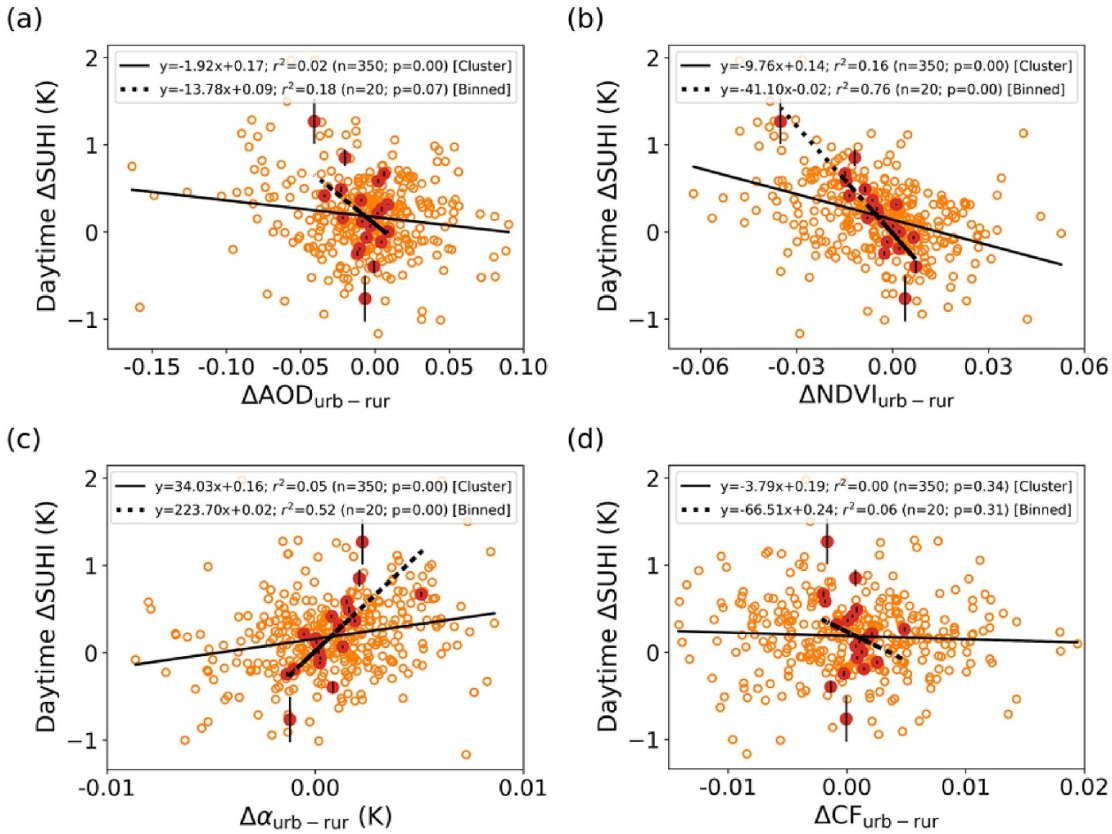

Figure 4. Statistical examination of daytime surface urban heat island (SUHI) enhancement. Sub-figures (a)–(d) show the correlations between daytime change in surface urban heat island (SUHI) (ΔSUHI) during the lockdown compared to the five year baseline and the respective change in urban–rural differential in aerosol optical depth ($\Delta AOD_{urb\text{-}rur}$), normalized difference vegetation index ($\Delta NDVI_{urb\text{-}rur}$), surface albedo ($\Delta\alpha_{urb\text{-}rur}$), and cloud fraction ($\Delta CF_{urb\text{-}rur}$), respectively. Each data point for the raw case (in orange) corresponds to an urban cluster. The lines of best fit are shown, and their corresponding equations (along with their sample sizes and *p*-values) are annotated. Values that are outside the 1–99 percentiles of the change in the predictor variables are considered outliers and not shown in these scatter plots. Correlations (in red) are also shown after binning every 5th percentile of ΔSUHI and the corresponding changes in the predictors. The vertical black lines show the standard deviation of ΔSUHI in each bin.

can enhance SUHI intensity. However, our statistical analysis does not support this hypothesis. Instead, the observed positive ΔSUHI is associated with the higher vegetation cover over rural areas. This control of vegetation cover on LST is further corroborated by the negative correlations between LST and NDVI for the urban and rural units (figure S11). The relatively weaker correlations for the cluster-level data in figure 4(b) compared to figures S9(a) and S11 (and previous studies [46, 47, 52]) is because we are dealing with differences of differences in figure 4(b) during a time of the year with low expected SUHI intensities (figure 3(d)), making the signal hard to isolate from the noise.

3.3. Perturbations to rural Background surface climate

The lack of large-scale continuous observations of meteorological variables in urban areas makes diagnosing these patterns for all-sky conditions difficult using *in-situ* data. Instead, we use the MERRA-2 reanalysis, which is observationally constrained by ground-level measurements of surface meteorology and satellite measurements of columnar AOD, and physically constrained by the model components [36]. MERRA-2 primarily represents the rural background since it does not incorporate urban land cover. Since, as suggested by the satellite-derived NDVI and α (figure 2), urban surfaces changed less than rural surfaces during the lockdown, the reanalysis data can be used to generate mechanistic insights about the SUHI enhancement.

The MERRA-2 reanalysis captures the direction of the changes in the region during the lockdown compared to satellite observations (table S3). Although the midday aerosol direct radiative effect in MERRA-2 decreases by almost 25% (from -78.4 ± 12.6 W m^{-2} to -58.7 ± 13.3 W m^{-2}) during the lockdown, with the potential to increase $K_{\downarrow}$ by 19.8 ± 5.1 W m^{-2}, we find an overall reduction in $K_{\downarrow}$ (-10.5 ± 39.8 W m^{-2}). This decrease in $K_{\downarrow}$ is due to the compensating effect of increased cloudiness during the lockdown, as well as the higher water vapor content in the atmospheric column, as seen from the higher near-surface relative humidity (table

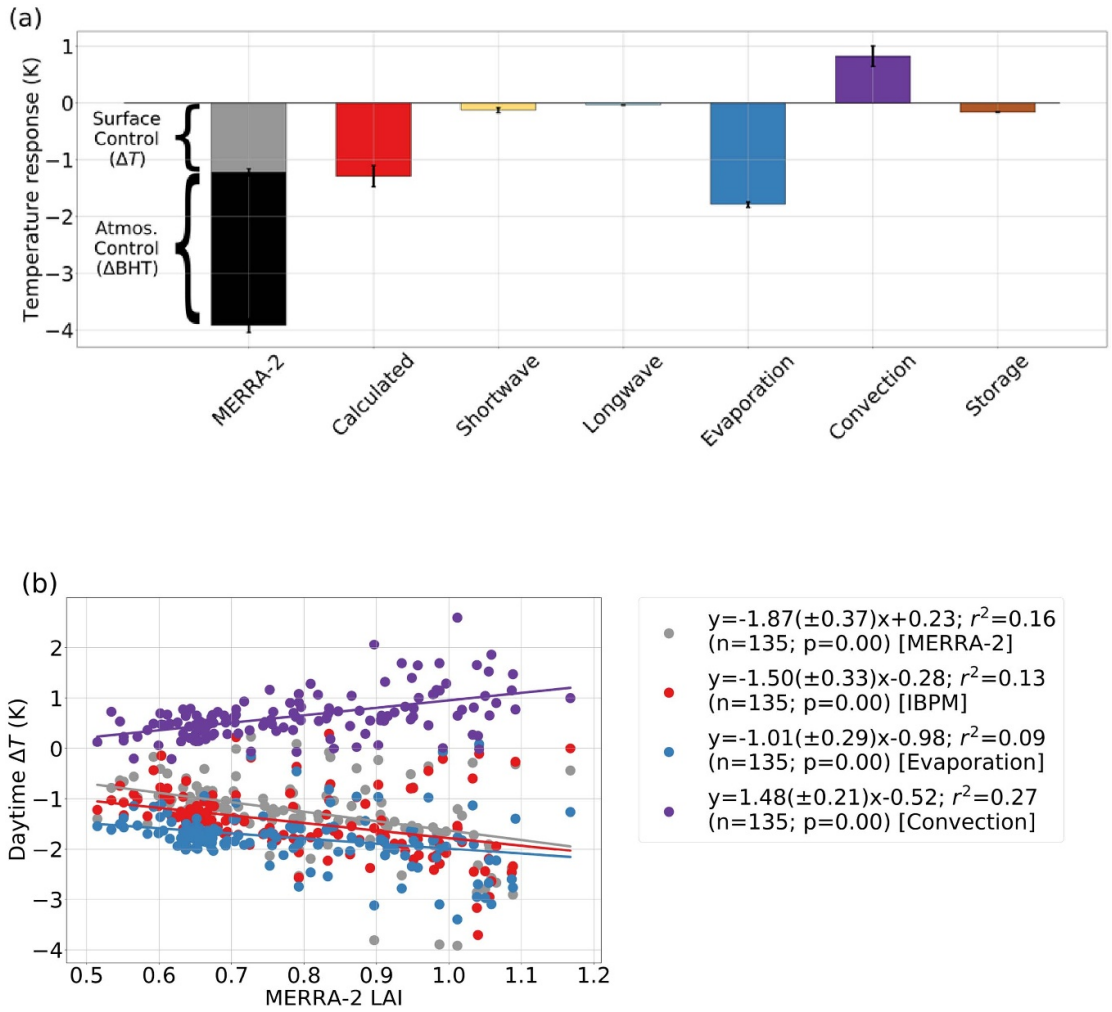

Figure 5. Contributions of different pathways to regional land surface temperature (LST) change. Sub-figure (a) shows contributions of all pathways, namely shortwave radiative forcing, longwave radiative forcing, evaporation, convection, and ground heat storage to the total calculated local temperature change (ΔT) in the Indo-Gangetic Basin during the lockdown compared to the five year baseline. The corresponding ΔT, ΔLST, and change in blending height temperature (ΔBHT) in MERRA-2 are also shown. The standard errors are displayed in all cases. Sub-figure (b) shows the correlations between the MERRA-2 grid-averaged leaf are index (LAI) and the corresponding ΔT from MERRA-2, the calculated ΔT using the IBPM framework, and the contributions to ΔT through the evaporative pathway and convective pathways. Each data point corresponds to a grid cell average. The lines of best fit are shown and the corresponding equations (including confidence bounds for the slopes of the lines, sample sizes, and *p*-values) are annotated. Values that are outside the 1–99 percentile of the total diagnosed local temperature change are considered outliers and not shown in the scatter plot.

S3). Overall, the total absorbed energy by the surface decreases slightly (-10.4 ± 32 W m^{-2}) during the lockdown despite the negative ΔAOD_{rur}.

Separating the contributions from both radiative and non-radiative pathways that can change LST reveals large evaporative cooling (-1.79 ± 0.05 K) during this period (figure 5(a)), which is expected if vegetation cover increased. The diagnosed and MERRA-2 calculated ΔT are similar in magnitude (-1.29 K versus -1.22 K) and in spatial distribution (figure 5(b)). MERRA-2 uses prescribed vegetation, with identical leaf area index (LAI; regional mean = ~0.79) for the two periods. However, since it is constrained by observed surface meteorology, it captures the decrease in Bowen ratio—the ratio of sensible heat flux (H) and λE—during midday (from 2.87 ± 3.02 for baseline to 1.24 ± 0.76 during the lockdown; table S3), which is an expected impact of surface greening. The higher precipitation, latent heat, cloud cover, and relative humidity point to a more intense hydrological cycle during the lockdown compared to regular years (table S3).

The satellite-observed negative $\Delta NDVI_{urb\text{-}rur}$ suggests that the increase in evaporative cooling during the lockdown was more for rural areas compared to urban areas. This would be true even if $NDVI_{urb}$ and $NDVI_{rur}$ had changed identically, since urban areas are generally more moisture-limited. Figure 5(b) shows the correlations of ΔT from MERRA-2, the IBPM calculations, and contributions due to evaporation and convection with LAI. The negative correlations between LAI and ΔT demonstrate a stronger cooling response during the lockdown over more densely vegetated surfaces. Here,

the lowest LAI grids represent relatively urbanized areas. The increasing positive temperature response through the convective pathway with LAI suggests that this is a negative feedback to the evaporative cooling [53]. This convective feedback can be understood either in terms of energy conservation or through evaporation-induced near-surface stability. A relative increase in λE under similar (or reduced) available energy requires a corresponding decrease in H. Alternatively, the additional evaporative cooling of the surface compared to the blending height renders the lower atmosphere relatively stable compared to the baseline period, impeding the dissipation of available energy via H.

Overall, ΔT is almost a third of ΔLST, with the other two-thirds attributable to atmospheric factors, including AOD and CF (figure 5(a)). The IBPM results show that the sum of the evaporative cooling and its convective feedback accounted for roughly 79% of the midday ΔT, while the evaporative cooling alone accounted for roughly 46% of the corresponding ΔLST (of -3.92 K). The land contribution to ΔLST found here is probably a lower bound estimate since there is strong coupling between the land and the atmosphere. For instance, enhanced surface evaporation due to the increase in vegetation cover would also increase low level cloudiness through condensation feedback [54], lowering both BHT and LST. A similar theoretical diagnosis is not possible for the urban surfaces explicitly since the MERRA-2 land cover dataset does not consider urban areas. Nonetheless, these results can explain the SUHI increase, as the implicit assumption is that the surface characteristics of the rural areas changed more than those of the urban areas during the lockdown period, which is reasonable given the time scale.

4. Discussion and conclusions

The UHI effect is traditionally viewed as an outcome of the replacement of the natural landscape by built-up structures. The consequences of this land cover change are simpler to define in the abstract than to measure in practice. While cities modify their local climate as they expand, the UHI intensity is usually quantified through space-for-time substitution using snapshot measurements in the urban area and for some rural reference. For the SUHI, how to define this rural reference remains a contentious issue [46, 55–57]. Generally, the urban–rural delineations are more clearly constructed for less sprawling cities with very little land management surrounding the city centers. Here, we show an example of a region of the world with high human intervention in both urban and rural areas, the interruption of which leads to the seemingly counter-intuitive enhancement of the SUHI during a period of low human activity. Thus, the COVID-19 lockdown period illustrates the importance of the rural reference on the SUHI intensity, as estimated using a traditional buffer-based method, during a perturbation scenario, the relevance of which has previously only been examined for the mean climate state in this region [17, 18, 58].

Our results can help contextualize a larger current discussion in the urban climate community on the utility of the UHI as a metric to examine urban public health [59–61]. The UHI intensity is the impact of urbanization on local temperature [62]. However, urban heat stress is dependent on the absolute temperature, or more accurately, a combination of temperature, humidity, and other factors [63]. As such, the relevance of UHI for urban public health can be misleading during certain times because enhancement in UHI intensity does not necessarily imply similar enhancement in heat stress (or even temperature) in urban areas. In agreement [64], argues that mitigating the UHI should not be the goal when addressing the public health consequences of urbanization. In theory, one can reduce the UHI intensity by increasing the rural temperature, which does not change the potential heat stress in the urban area. Here, we see something similar occurring, with the SUHI increasing due to rural areas cooling down more than the urban core between the baseline and the lockdown periods, rather than due to an increase in urban temperature. However, this is only the temporal perspective. From the spatial perspective, it is also true that residents moving from rural to urban regions in the IGB were exposed to higher temperatures than they would have had they remained in rural areas. This separation of the temporal and spatial perspectives is critical to reconciling the debate in the community. The criticisms of UHI as a metric primarily pertain to the total impact of temperature on human health in urban areas. In contrast, since the UHI is an abstract isolation of the contribution to that temperature from urbanization, it remains theoretically important, assuming we establish a more consistent definition of the rural reference to facilitate accurate inter-urban and inter-study comparisons.

Lastly, our finding demonstrates the importance of human–land–atmosphere coupling on the regional climate over South Asia as a whole. Agricultural practices in this region strongly control the vegetation phenology of the croplands, modulating how energy is partitioned and dissipated from the surface through non-radiative means (figure 3(c)). As seen here, the importance of these non-radiative components on the LST is apparent, even when input energy to the system is relatively stable, providing large-scale observational evidence of previously modeled results [54]. Over 88% of the landmass in North India is agricultural (figure S1(b)). Therefore, an increase in surface vegetation due to agriculture can lead to large regional cooling, modify cloud formation, and lower

tropospheric stability. Moreover, enhanced evaporative cooling over the Indian landmass during the monsoon onset period (as seen here) can also perturb the land–sea thermal gradient—a major driver of monsoonal wind circulation [65]. Our study puts forth important observational evidence of human-induced control on surface climate, which strengthens the need for the ongoing efforts to explicitly include these in earth system models to better predict long-term climate change [66, 67]. For the UHI, the inclusion of human dynamics can help constrain its future estimates, since urban and rural areas are expected to change differently in future scenarios [68].

Although our two-pronged approach using satellite observations and reanalysis product demonstrates the consistency of these perturbations, a few uncertainties remain. First, since 2020 was wetter than the baseline years (table S3), the NDVI perturbations seen during lockdown may not have been solely due to the well-documented delay in harvesting in this region [16]. The lockdown-induced anthropogenic pause could influence the natural variability, cloud cover, and rainfall [69, 70], and in turn also affect the NDVI/LST. Regardless, the large, standardized anomaly in $NDVI_{rur}$ during the lockdown, seen in figure 3(c), strongly suggests that the lockdown played a role. The higher $\Delta NDVI_{rur}$ (compared to $\Delta NDVI_{urb}$) and $\Delta SUHI$ is also see when using 18 year (2003–2019) baseline from MODIS Aqua measurements (figures S12(a) and (b)). Moreover, NDVI differences are seen at urban-to-urban periphery scale (5–30 km), which is much smaller than the inherent spatial scale of the anticipated natural variability. Second, since the perturbations are small in magnitude, sensor noise could account for some of the variability. Our results are qualitatively replicated when we calculate the relevant variables from the MODIS Terra satellite (figures S12(c) and (d)), which has a different sensor and equatorial overpass time (∼10:30 am), indicating that the perturbations are robust and cannot be just random noise from one sensor. Third, since our study deals with regional changes using coarse satellite observations, we neither fully examine the perturbations for individual urban clusters, which can vary from the mean changes (figures S4(a) and (b)), nor characterize intra-urban distributions. Some of these limitations can be addressed with the development of better parameterized models for this region with explicit irrigation schemes, which can clearly isolate the impact of the agricultural cycle on regional climate.

Data availability statement

The data that support the findings of this study are available upon reasonable request from the authors.We acknowledge the Yale Institute for Biospheric Studies for a grant on studying aerosol-UHI interactions.

Acknowledgments

TC acknowledges the Yale Institute for Biospheric Studies for a grant on studying aerosol-UHI interactions. CS would like to thank Department of Science and Technology, Government of India, for the DST Start-Up Grant 2020 [Ref. No. **SRG/2020/001658**].

ORCID iDs

TC Chakraborty https://orcid.org/0000-0003-1338-3525
Chandan Sarangi https://orcid.org/0000-0002-4850-5118
Xuhui Lee https://orcid.org/0000-0003-1350-4446

References

[1] Pielke Sr R A, Marland G, Betts R A, Chase T N, Eastman J L, Niles J O, Niyogi D D S and Running S W 2002 The influence of land-use change and landscape dynamics on the climate system: relevance to climate-change policy beyond the radiative effect of greenhouse gases *Phil. Trans. R. Soc.* A **360** 1705–19
[2] Lawrence D M *et al* 2016 The Land Use Model Intercomparison Project (LUMIP) contribution to CMIP6: rationale and experimental design *Geosci. Model Dev.* **9** 2973–98
[3] Rutz C *et al* 2020 Covid-19 lockdown allows researchers to quantify the effects of human activity on wildlife *Nat. Ecol. Evol.* **4** 1156–9
[4] Dey S and di Girolamo L 2011 A decade of change in aerosol properties over the Indian subcontinent *Geophys. Res. Lett.* **38**
[5] Koster R D *et al* 2004 Regions of strong coupling between soil moisture and precipitation *Science* **305** 1138–40
[6] Guidelines, Ministry of Home Affairs, Government of India 2020 (available at: www.mha.gov.in/sites/default/files/Guidelines.pdf) (Accessed 27 December 2020)
[7] Seto K C, Güneralp B and Hutyra L R 2012 Global forecasts of urban expansion to 2030 and direct impacts on biodiversity and carbon pools *Proc. Natl Acad. Sci.* **109** 16083–8
[8] Siderius C, Hellegers P, Mishra A, van Ierland E and Kabat P 2014 Sensitivity of the agroecosystem in the Ganges basin to inter-annual rainfall variability and associated changes in land use *Int. J. Climatol.* **34** 3066–77
[9] Sarangi C, Tripathi S, Qian Y, Kumar S and Leung L R 2018 Aerosol and urban land use effect on rainfall around cities in Indo-Gangetic Basin from observations and cloud resolving model simulations *J. Geophys. Res.* **123** 3645–67
[10] Barton E J *et al* 2019 A case study of land–atmosphere coupling during monsoon onset in northern India *Q. J. R. Meteorol. Soc.* **146** 2891–905
[11] Oke T R 1982 The energetic basis of the urban heat island *Q. J. R. Meteorol. Soc.* **108** 1–24
[12] Ranjan A K, Patra A K and Gorai A K 2020 Effect of lockdown due to SARS COVID-19 on aerosol optical depth (AOD) over urban and mining regions in India *Sci. Total Environ.* **745** 141024
[13] Li H, Meier F, Lee X, Chakraborty T, Liu J, Schaap M and Sodoudi S 2018 Interaction between urban heat island and urban pollution island during summer in berlin *Sci. Total Environ.* **636** 818–28
[14] Cao C, Lee X, Liu S, Schultz N, Xiao W, Zhang M and Zhao L 2016 Urban heat islands in china enhanced by haze pollution *Nat. Commun.* **7** 1–7

[15] Zhao L, Lee X, Smith R B and Oleson K 2014 Strong contributions of local background climate to urban heat islands *Nature* **511** 216–9
[16] Rawal V, Kumar M, Verma A and Pais J 2020 Covid-19 lockdown: impact on agriculture and rural economy *Soc. Soc. Econ. Res.* (https://www.networkideas.org/wp-content/uploads/2020/06/sserwp2003.pdf)
[17] Chakraborty T, Sarangi C and Tripathi S N 2017 Understanding diurnality and inter-seasonality of a sub-tropical urban heat island *Bound.-Layer Meteorol.* **163** 287–309
[18] Kumar R, Mishra V, Buzan J, Kumar R, Shindell D and Huber M 2017 Dominant control of agriculture and irrigation on urban heat island in India *Sci. Rep.* **7** 1–10
[19] Chakraborty T, Sarangi C, Krishnan M, Tripathi S N, Morrison R and Evans J 2019 Biases in model-simulated surface energy fluxes during the Indian monsoon onset period *Bound. Layer Meteorol.* **170** 323–48
[20] Venter Z S, Aunan K, Chowdhury S and Lelieveld J 2020 Covid-19 lockdowns cause global air pollution declines *Proc. Natl Acad. Sci.* **117** 18984–990
[21] le Quéré C *et al* 2020 Temporary reduction in daily global CO_2 emissions during the COVID-19 forced confinement *Nat. Clim. Change* **10** 647–53
[22] Turner A G *et al* 2019 Interaction of convective organization with monsoon precipitation, atmosphere, surface and sea: the 2016 INCOMPASS field campaign in India *Q. J. R. Meteorol. Soc.* **146** 2828–52
[23] Pesaresi M *et al* 2013 A global human settlement layer from optical HR/VHR RS data: concept and first results *IEEE J. Sel. Top. Appl. Earth Obs. Remote Sens.* **6** 2102–31
[24] Wan Z 2007 Collection-5 MODIS land surface temperature products users' guide *ICESS* (Santa Barbara: University of California)
[25] Pagano T S and Durham R M 1993 Moderate resolution imaging spectroradiometer (MODIS) *Sensor Systems for the Early Earth Observing System Platforms* vol 1939 (International Society for Optics and Photonics) pp 2–17
[26] Remer L A *et al* 2006 Algorithm for remote sensing of tropospheric aerosol from MODIS: collection 005 *Natl Aeronaut. Space Adm.* **1490**
[27] Veefkind J *et al* 2012 Tropomi on the ESA Sentinel-5 precursor: a GMES mission for global observations of the atmospheric composition for climate, air quality and ozone layer applications *Remote Sens. Environ.* **120** 70–83
[28] Theeuwes N E, Barlow J F, Teuling A J, Grimmond C S B and Kotthaus S 2019 Persistent cloud cover over mega-cities linked to surface heat release *npj Clim. Atmos. Sci.* **2** 1–6
[29] Strahler A H, Muller J, Lucht W, Schaaf C, Tsang T, Gao F, Li X, Lewis P and Barnsley M J 1999 MODIS BRDF/albedo product: algorithm theoretical basis document version 5.0 *MODIS Doc.* **23** 42–7
[30] Rizwan A M, Dennis L Y and Chunho L 2008 A review on the generation, determination and mitigation of urban heat island *J. Environ. Sci.* **20** 120–8
[31] Chakraborty T, Hsu A, Manya D and Sheriff G 2020 A spatially explicit surface urban heat island database for the United States: characterization, uncertainties, and possible applications *ISPRS J. Photogramm. Remote Sens.* **168** 74–88
[32] Bontemps S *et al* 2013 Consistent global land cover maps for climate modelling communities: current achievements of the ESA's land cover CCI *Proc. ESA Living Planet Symp. (Edimburgh)* pp 9–13
[33] Rouse J, Haas R, Schell J and Deering D 1973 Monitoring the vernal advancement and retrogradation (green wave effect) of natural vegetation *Prog. Rep. RSC* 1978-1 (College Station 93: Remote Sensing Center, Texas A&M Univ.)
[34] Gorelick N, Hancher M, Dixon M, Ilyushchenko S, Thau D and Moore R 2017 Google Earth Engine: planetary-scale geospatial analysis for everyone *Remote Sens. Environ.* **202** 18–27
[35] Hersbach H *et al* 2020 The ERA5 global reanalysis *Q. J. R. Meteorol. Soc.* **146** 1999–2049
[36] Gelaro R *et al* 2017 The modern-era retrospective analysis for research and applications, version 2 (MERRA-2) *J. Clim.* **30** 5419–54
[37] Qu Y, Liang S, Liu Q, He T, Liu S and Li X 2015 Mapping surface broadband albedo from satellite observations: a review of literatures on algorithms and products *Remote Sens.* **7** 990–1020
[38] Chakraborty T, Hsu A, Manya D and Sheriff G 2019 Disproportionately higher exposure to urban heat in lower-income neighborhoods: a multi-city perspective *Environ. Res. Lett.* **14** 105003
[39] Chakraborty T and Lee X Large differences in diffuse solar radiation in current-generation gridded products (under review)
[40] Breiman L 2001 Random forests *Mach. Learn.* **45** 5–32
[41] Xu Q-S and Liang Y-Z 2001 Monte Carlo cross validation *Chemometr. Intell. Lab. Syst.* **56** 1–11
[42] Lee X *et al* 2011 Observed increase in local cooling effect of deforestation at higher latitudes *Nature* **479** 384–7
[43] Chakraborty T and Lee X 2019 Land cover regulates the spatial variability of temperature response to the direct radiative effect of aerosols *Geophys. Res. Lett.* **46** 8995–9003
[44] Mahrt L 2000 Surface heterogeneity and vertical structure of the boundary layer *Bound.-Layer Meteorol.* **96** 33–62
[45] Sarangi C, Tripathi S, Mishra A, Goel A and Welton E 2016 Elevated aerosol layers and their radiative impact over Kanpur during monsoon onset period *J. Geophys. Res.* **121** 7936–57
[46] Peng S, Piao S, Ciais P, Friedlingstein P, Ottle C, Breon F-M, Nan H, Zhou L and Myneni R B 2012 Surface urban heat island across 419 global big cities *Environ. Sci. Technol.* **46** 696–703
[47] Chakraborty T and Lee X 2019 A simplified urban-extent algorithm to characterize surface urban heat islands on a global scale and examine vegetation control on their spatiotemporal variability *Int. J. Appl. Earth Obs. Geoinf.* **74** 269–80
[48] Lau K, Kim M and Kim K 2006 Asian summer monsoon anomalies induced by aerosol direct forcing: the role of the Tibetan Plateau *Clim. Dyn.* **26** 855–64
[49] Bollasina M A, Ming Y and Ramaswamy V 2011 Anthropogenic aerosols and the weakening of the South Asian summer monsoon *science* **334** 502–5
[50] Ackerman A S, Toon O, Stevens D, Heymsfield A, Ramanathan V and Welton E 2000 Reduction of tropical cloudiness by soot *Science* **288** 1042–7
[51] Teuling A J, Taylor C M, Meirink J F, Melsen L A, Miralles D G, van Heerwaarden C C, Vautard R, Stegehuis A I, Nabuurs G-J and de Arellano J V G 2017 Observational evidence for cloud cover enhancement over western European forests *Nat. Commun.* **8** 1–7
[52] Yue W, Xu J, Tan W and Xu L 2007 The relationship between land surface temperature and NDVI with remote sensing: application to Shanghai Landsat 7 ETM+ data *Int. J. Remote Sens.* **28** 3205–26
[53] Gerken T, Ruddell B L, Yu R, Stoy P C and Drewry D T 2019 Robust observations of land-to-atmosphere feedbacks using the information flows of FLUXNET *npj Clim. Atmos. Sci.* **2** 1–10
[54] Ban-Weiss G A, Bala G, Cao L, Pongratz J and Caldeira K 2011 Climate forcing and response to idealized changes in surface latent and sensible heat *Environ. Res. Lett.* **6** 034032
[55] Martin P, Baudouin Y and Gachon P 2015 An alternative method to characterize the surface urban heat island *Int. J. Biometeorol.* **59** 849–61
[56] Martin-Vide J, Sarricolea P and Moreno-garcía M C 2015 On the definition of urban heat island intensity: the 'rural' reference *Front. Earth Sci.* **3** 24

[57] Li K, Chen Y, Wang M and Gong A 2019 Spatial-temporal variations of surface urban heat island intensity induced by different definitions of rural extents in China *Sci. Total Environ.* **669** 229–47
[58] Shastri H, Barik B, Ghosh S, Venkataraman C and Sadavarte P 2017 Flip flop of day-night and summer-winter surface urban heat island intensity in India *Sci. Rep.* **7** 1–8
[59] Manoli G, Fatichi S, Schläpfer M, Yu K, Crowther T W, Meili N, Burlando P, Katul G G and Bou-Zeid E 2019 Magnitude of urban heat islands largely explained by climate and population *Nature* **573** 55–60
[60] Martilli A *et al* 2020 Summer average urban-rural surface temperature differences do not indicate the need for urban heat reduction (https://doi.org/10.31219/osf.io/8gnbf)
[61] Manoli G, Fatichi S, Schläpfer M, Yu K, Crowther T W, Meili N, Burlando P, Katul G and Zeid E B 2020 Reply to Martilli *et al.* (2020): summer average urban-rural surface temperature differences do not indicate the need for urban heat reduction (https://doi.org/10.31219/osf.io/mwpna)
[62] Manoli G, Fatichi S, Bou-Zeid E and Katul G G 2020 Seasonal hysteresis of surface urban heat islands *Proc. Natl Acad. Sci.* **117** 7082–9
[63] Lemonsu A, Viguie V, Daniel M and Masson V 2015 Vulnerability to heat waves: impact of urban expansion scenarios on urban heat island and heat stress in Paris (France) *Urban Clim.* **14** 586–605
[64] Martilli A, Krayenhoff E S and Nazarian N 2020 Is the urban heat island intensity relevant for heat mitigation studies? *Urban Clim.* **31** 100541
[65] Roxy M K, Ritika K, Terray P, Murtugudde R, Ashok K and Goswami B 2015 Drying of Indian subcontinent by rapid Indian ocean warming and a weakening land-sea thermal gradient *Nat. Commun.* **6** 1–10
[66] Beckage B *et al* 2018 Linking models of human behaviour and climate alters projected climate change *Nat. Clim. Change* **8** 79–84
[67] Donges J F *et al* 2020 Earth system modeling with endogenous and dynamic human societies: the Copan: core open world–earth modeling framework *Earth Syst. Dyn.* **11** 395–413
[68] Oleson K 2012 Contrasts between urban and rural climate in CCSM4 CMIP5 climate change scenarios *J. Clim.* **25** 1390–412
[69] Latha R, Murthy B S, Sandeepan B S, Bhanage V, Rathod A, Tiwari A, Beig G and Singh S 2021 Propagation of cloud base to higher levels during Covid-19-lockdown *Sci. Total Environ.* **759** 144299
[70] Timmermann A, Lee S, Chu J, Chung E and Lee J 2020 COVID-19-related drop in anthropogenic aerosol emissions in China and corresponding cloud and climate effects (https://doi.org/10.31223/osf.io/z5dm8)